Ferroelectric State in an α-Nd2 WO6 Polymorph Stabilized in a Thin Film

Thomas Carlier, Marie-Hélène Chambrier, Antonio da Costa, Florent Blanchard, Thibaud Denneulin, Manon Letiche, Pascal Roussel, Rachel Desfeux, Anthony Ferri

To cite this version:

Thomas Carlier, Marie-Hélène Chambrier, Antonio da Costa, Florent Blanchard, Thibaud Denneulin, et al.. Ferroelectric State in an α-Nd2 WO6 Polymorph Stabilized in a Thin Film. Chemistry of Materials, 2020, 32 (17), pp.7188-7200. ⟨10.1021/acs.chemmater.0c01405⟩. ⟨hal-02933289⟩

HAL Id: hal-02933289
https://hal.science/hal-02933289v1

Submitted on 13 Nov 2023

Ferroelectric state in a α-Nd_2WO_6 polymorph stabilized in thin film

Thomas Carlier [a,c], Marie-Hélène Chambrier [a*], Antonio Da Costa [a], Florent Blanchard [b], Thibaud Denneulin [d, e], Manon Létiche [a,f], Pascal Roussel [b], Rachel Desfeux [a], Anthony Ferri [a]

[a] Univ. Artois, CNRS, Centrale Lille, Univ. Lille, UMR 8181 – UCCS – Unité de Catalyse et Chimie du Solide, F-62300 Lens, France
[b] Univ. Lille, CNRS, Centrale Lille, Univ. Artois, UMR 8181 – UCCS – Unité de Catalyse et Chimie du Solide, F-59000 Lille, France
[c] HORIBA FRANCE S.A.S., Boulevard Thomas Gobert, Passage Jobin Yvon, 91120 Palaiseau, France
[d] Ernst Ruska-Centre for Microscopy and Spectroscopy with Electrons and Peter Grünberg Institute, Forschungszentrum Jülich, 52425 Jülich, Germany
[e] CEMES, CNRS, 29 rue Jeanne Marvig, 31055 Toulouse, France
[f] Institut Laue Langevin (ILL), F-38042 Grenoble, France

ABSTRACT: Taking advantage of strain engineering, Nd_2WO_6 (NdWO) thin films have been successfully grown on (001)-oriented $SrTiO_3$ single-crystal substrates by pulsed laser deposition. High-resolution X-ray diffraction characterizations highlight the stabilization of a new orthorhombic ($Pm2_1n$) NdWO polymorphic form, isostructural to α-La_2WO_6. Reciprocal Space Mappings have been used in the determination of the NdWO thin film structure. Coupled to the 2θ-ω X-ray patterns, the cell parameters were calculated: a = 16.34(5) Å, b = 5.46(5) Å, c = 8.68(1) Å. X-ray-diffraction pole-figure measurements evidence the crystallographic relationships between the film and substrate: $[100]_{NdWO} \parallel [110]_{STO}$, $[010]_{NdWO} \parallel [1\bar{1}0]_{STO}$ and $[001]_{NdWO} \parallel [001]_{STO}$. Both X-ray diffraction and transmission electron microscopy studies reveal the existence of (510)-oriented crystallites with respect to the plane of the substrate mainly at the interface film/substrate and dispersed in the (001)-NdWO matrix. In addition, robust piezoelectricity and ferroelectricity are revealed at room temperature through both local hysteresis loops and domain manipulation experiments using piezoresponse force microscopy technique. Typical polarization retention behaviour associated to specific nanoscale conduction are in good agreement with classical ferroelectric phenomenon in oxide materials. The successful observation of piezo-/ferroelectricity at room temperature in innovative strain-stabilized α-NdWO thin films paves the way for new lead-free functional materials devoted to numerous applications, including actuators, sensors, or non-volatile memory devices.

INTRODUCTION

Since World War II, advanced electronic devices based on piezoelectric and ferroelectric materials attracted a lot of attention and represent an important part of industrial-business and innovations, taking in mind the fact that piezo-/ferroelectric applications areas are wide ranging from consumer devices to high technology industries: laptops, sonars, frequency filters, gas sensors, data storage systems (Ferroelectric Random Access Memories (FeRAMs)), etc. Moreover, promising and impending technological developments such as energy harvesting, geothermal power plant sensors, aerospace, miniaturization still keep piezo-/ferroelectric materials highly attractive. Since the 40's, lead zirconate-titanate $Pb(Zr,Ti)O_3$ (PZT), [1,2]$(Pb,La)(Zr,Ti)O_3$ (PLZT) [3] or $x$$Pb(MgNb)O_3$-(1–$x$)$PbTiO_3$ (PMN-PT) [4] to cite the main ones of the well-known lead-based perovskite type family have been in the first place on the market of such electromechanical materials due to exceptional piezoelectric coefficient and polarization at room temperature. [5, 6, 7] It is interesting to note that since the 70's, plenty of patents for Pb-containing relaxor based on multi-layer piezo-/ferroelectric ceramic capacitor devices have been filed. [8]

However, in reference to the European Union legislations, REACH (*Registration, Evaluation, Authorization and Restriction of Chemicals*) classification, connected to the environmental concerns, has decreed that even if lead-based substances are still allowed for the moment, they have to be progressively replaced by less toxic substances. [9, 10]

In this context, new investigations have been conducted, mainly based on two strategies: either optimize well-known piezoelectric materials such as $BaTiO_3$ (BTO) [11] and $K_xNa_{1-x}NbO_3$ (KNN) [12], or explore new systems. Our approach belongs to this last option with the aim to discover new lead-free piezo-/ferroelectric compounds.

In the present work, we focus on lanthanide tungstate Ln_2WO_6 systems for different well-targeted reasons: i) some polymorphs are noncentro-symmetric and therefore susceptible to present ferroelectricity, ii) some tungsten bronze $K_xW_2O_6$ are already known to form a ferroelectric class and also iii) dozen of papers deals with Bi_2WO_6 compound and its ferroelectric properties.

Even if studies of A_2O_3-MO_3 (A = Ln^{3+}, Bi^{3+}, Y^{3+}, Fe^{3+}, Sc^{3+} and M = W^{6+}, Mo^{6+}) phase diagram were intensive in 70's in order to determine their structure, nowadays some of these phase diagrams still remain incomplete in terms of characterization properties. Concerning piezo-/ferroelectric properties, only a few works and even patents have been written for $A_2M_3O_{12}$ (A = Gd, Tb and Eu , Y; M = W and Mo).[13, 14]

On the other hand, Ln_2O_3-WO_3 systems are interesting because of the low cost of both lanthanide and tungsten elements, combined to the low toxicity of these elements, which anticipates both European decrees as previously reported and industrial constraints. [9; 10] In terms of piezoelectric properties, lanthanide elements are stimulating owing their high polarizability (5.01 $Å^3$ for neodymium for instance). [15]

Concerning Ln_2WO_6 compounds, depending on the lanthanide radius, three different tungstate structures are observed according to the temperature and the exact method of synthetic preparation. [16, 17, 18, 19, 20, 21, 22, 23]

La_2WO_6 presents two polymorphic structures depending on the temperature: i) the low temperature form, β-La_2WO_6, crystallizes in the space group $P2_12_12_1$ (n°19) with cell parameters a = 7.5196(1) Å, b = 10.3476(1) Å, c = 12.7944(2) Å, **[24]** ii) the high temperature form, **[25]** α-La_2WO_6, crystallizes in the space group $Pm2_1n$ (n°31) with cell parameters a = 16.5531(1) Å, b = 5.5200(1) Å, c = 8.8833(1) Å. A first order phase transition between beta and alpha occurs at 1440°C. The structure for the α-La_2WO_6 phase is closely related to the Scheelite one. Recently, piezoelectricity and ferroelectricity within this compound were evidenced by our group when stabilized in thin film form on $SrTiO_3$ and $LaAlO_3$ substrates. [26, 27]

On the one hand, Ln_2WO_6 compounds with large cations (Ln = Ce to Dy) usually crystallize in a monoclinic fluorine type-superstructure ($C\frac{2}{c}$; $a_M \approx 3a_F$; $b_M \approx 2b_F$; $c_M \approx c_F$ and $\beta \approx 107.7°$). [28] On the other hand, for the smallest cations (Ln = Ho to Lu) it results in a $P\frac{2}{c}$ space group Scheelite-type superstructure with following relationships: $\overrightarrow{a_m} \approx \overrightarrow{b_{sch}}$ - $\overrightarrow{a_{sch}}$; $\vec{b}_m = \frac{\overrightarrow{c_{sch}}}{2}$; $\overrightarrow{c_m} \approx 2\overrightarrow{a_{sch}} + \overrightarrow{b_{sch}}$; $\beta_m \approx 108°$.[29, 30]

At high temperature, all the Ln_2WO_6 compounds with Ln = Ce to Lu undergo a phase transition (>1500°C) to a tetragonal compound.

Concerning Nd_2WO_6, Yoshimura *et al.* have reported another metastable phase between the low and high temperature prototypes in addition to the phase transition close to 1430°C. [31] The low temperature form crystallizes in the space group $C\frac{2}{c}$ (n°15) with cell parameters a = 5.55(1) Å, b = 11.38(1) Å, c = 15.86(1) Å, β = 107.7°. The structure consists of two strongly distorted polyhedra: i) tungsten atoms are surrounded by five oxygen atoms, which build up an isolated trigonal bipyramid $[WO_5]^{-4}$; ii) neodymium atoms are forming $[LnO_8]^{-10}$ units (**Figure 1a**). The "intermediate temperature" polymorph observed between 1430°C and 1450°C is metastable and has been described in the orthorhombic system with the space group $P2_12_12_1$ (n°19) and cell parameters a = 5.536(1) Å, b = 9.231(1) Å, c = 10.170(1) Å. [16,32] This allotropic variety can be described with distorted isolated $[WO_6]$ and two different types of polyhedra for the neodymium: a square-triangle polyhedron $[Nd(1)O_7]$ and a monocapped trigonal prism $[Nd(2)O_6]$ (**Figure 1b**). [33] Finally, the third polymorph at high temperature (T>1450°C), has been first indexed by Yoshimura *et al.* in a tetragonal cell closely related to an ordered fluorite ($a_T \approx a_F$ = 5.426Å; $c_T \approx c_F$ = 8.695Å) (**Figure 1c**). [31, 34]

Yoshimura *et al.* and Efremov have noticed that all Ln_2WO_6 compounds, [31; 23] have the same high temperature structural type even if low temperature polymorphs are different. Later, Tyulin *et al.* solved the structure of $Nd_{1.2}Lu_{0.8}WO_6$ which is isostructural to the Ln_2WO_6 high temperature form; [35] it crystallizes in the space group $P\bar{4}2_1m$ (n°113) with cell parameters a = 5.276(1) Å; c = 8.658(1) Å. The structure consists of large isolated $[WO_6]$ octahedra (**figure 1c**), while the neodymium atoms are in cubic coordination.

In our work, we focus on the growth of Nd_2WO_6 thin film by means of Pulsed Laser Deposition (PLD) on (001)-oriented $SrTiO_3$ (STO) substrate. Advanced microstructural characterizations carried out by X-Ray Diffraction (XRD) and Transmission Electron Microscopy (TEM) reveal the stabilization of a new Nd_2WO_6 polymorph, hereafter labelled alpha. Nanoscale ferroelectricity is highlighted in this new oxide thin film by carefully investigating electrical properties using Atomic Force Microscopy tools and, more specifically, the Piezoresponse Force Microscopy (PFM) and Conductive-AFM (c-AFM) modes.

EXPERIMENTAL METHODS

A Nd_2WO_6 ceramic pellet, 1 inch in diameter and 5 mm-thick, was used as target for laser ablation. The ceramic was prepared by solid-state reaction route method, mixing dried oxides Nd_2O_3 and WO_3 (Sigma Adrich, purities of 99.9%) weighted in stoichiometric proportions. Twice, with an intermediate grinding, the mixture was heated at 1350°C in air for one night. The resulting powder was then ground, pressed in the form of a disc using an uni-axial press, sintered up to 1450°C for 12h in air and slowly cooled down to room temperature. The XRD pattern confirms the synthesis of a pure powder of the low temperature polymorph of Nd_2WO_6 that was afterward used as target. [16]

The depositions as thin film form by PLD were carried out with a Compex Pro 102 KrF excimer laser (λ = 248 nm) on (001)-oriented STO single-crystal substrates (Crystal GmbH, Germany). The fluence was adjusted to 2 J/cm^2 and the deposition rate was 2 Hz. The target-substrate distance was adjusted to d = 4.5 cm. All substrates were first ultrasonically cleaned in ethanol for 5 minutes, and then dried. The pressure in the pulsed-laser chamber was lowered down to 10^{-4} Pa. Then, the substrate temperature was raised through a 10°C/min step elevation to the growth temperature, *i.e.* 900°C under a dynamical O_2 pressure of 10^{-1} mbar, while the deposition corresponds to 12000 laser-pulse shots corresponding to a film thickness around 200 nm. Finally, O2 gas was introduced into the chamber (200 mBar) and the film was slowly cooled down to room temperature.

The bulk-powder X-ray diffractograms were obtained using a Rigaku Ultima IV equipped with a Cu-anode X-ray tube ($\lambda K_\alpha = 1.5418$ Å). The thin films crystalline nature (indexation, rocking curves and Reciprocal Space Maps (RSMs)) were characterized using a Rigaku SmartLab X-ray diffractometer equipped with a 9 kW rotating anode X-ray generator and a copper anode. For 2θ-ω and rocking curves analysis, ϕ-scan and RSMs, a high resolution configuration was used: the X-Ray beam was made parallel with a cross-beam optics and monochromatized with a double Ge (220) monochromator. In this study all the (2θ-ω) scans were performed in the range of 10-90°, with a step size of 0.02° and a 1°/min speed whereas the Φ-scan was acquired in the range of -10-360°, with a step size of 0.4° and a 40°/min speed. Pole figure measurements were made in medium resolution configuration, *i.e.* without the monochromator ($\lambda K_\alpha = 1.5418$ Å) using a 0.5° grazing incidence and an in-plane geometry.

The TEM images were obtained using a Hitachi HF-3300 equipped with a cold field emission gun operated at 300 kV, an image aberration corrector (CEOS B-COR) and a 4k×4k camera (Gatan Oneview). Cross-section electron transparent thin foils were prepared using a dual beam machine (scanning electron microscope and focused gallium ion beam) FEI Helios. High resolution TEM images were processed using the Digital Micrograph software (Gatan). A color-coded map was created to show the distribution of two domain orientations in the film. A Fourier transform of the HRTEM image was first calculated. Circular masks were applied to isolate spots corresponding to a single domain orientation and the inverse Fourier transform was then calculated. The same operation was repeated twice for the second domain orientation and for the substrate. The three complex images obtained after inverse Fourier transform were used to create a RGB composite image where the modulus of each image is affected to a different color. Lattice deformation maps were calculated from the HRTEM image using geometrical phase analysis. [36] Fourier transform operations and masks in Fourier space were used to reconstruct two phase images corresponding to two sets of non-colinear reciprocal lattice vectors. Horizontal (in-plane), vertical (out-of-plane) and shear deformation maps were calculated from the gradient of the phase images. The local deformation $E_{(x,y)}$ at a position (x,y) in the map is defined $E_{(x,y)}=(d_{(x,y)}-d_{STO})/d_{STO}$ where d_{STO} is the average interplanar distance in the $SrTiO_3$ substrate and $d_{(x,y)}$ is the local interplanar distance. The spatial resolution in the deformation maps is 5 nm and the precision is 2%.

PFM and c-AFM experiments were performed with an AFM microscope (MFP-3D, Asylum Research/Oxford Instruments) at room temperature and under ambient conditions to get access to the local electrical properties. In this case, semi-conductive (001)-oriented STO:Nb (1.4 at%) substrates were used. Ti/Ir-coated tip and cantilever with a nominal ~2.8 $N.m^{-1}$ spring constant (ASYELEC-01, Asylum Research) were used. PFM analysis were carried out by using dual AC resonance tracking (DART) mode to enhance the detected electromechanical signal. [37] PFM in spectroscopic mode was conducted by applying a driving voltage of 2V to the local probe. The piezoloops were recorded in remnant mode, *i.e.* voltage pulses are applied to the active layer and the PFM signal is measured at zero field. Such measurements promote electromechanical activity against electrostatic interaction. [38] Poling experiments were performed by applying DC voltages of ±10 V to the probe tip. Further details can be found elsewhere. [39] For c-AFM measurements, the probe tip was grounded and the bias voltage was applied to the bottom electrode.

RESULTS AND DISCUSSION

Structural characterizations

In order to characterize the crystalline quality of the films, 2θ-ω diffractograms were collected (see **Figure 2a**). Several well-defined peaks are observed, corresponding to both substrate (in black) and film (in red). As already reported in the literature and summarized in the introduction part of this paper, depending on the temperature, three allotropic varieties of Nd_2WO_6 can be stabilized as long as powders are concerned (reminder: low temperature form is monoclinic $C\frac{2}{c}$ with a = 5.55(1) Å, b = 11.38(1) Å, c = 15.86(1) Å, β = 107.7, it is orthorhombic $P2_12_12_1$ a = 5.536(1) Å, b = 9.231(1) Å, c = 10.170(1) Å at intermediate temperature and finally tetragonal $P\bar{4}2_1m$, a = 5.426(2) Å; c = 8.695(2) Å for the high temperature polymorph). By comparison with ICDD-PDF cards, we identified a preferential growth direction of the film (6 harmonic diffraction peaks series) with a parameter around 8.68 Å, *i.e.* either the $\vec{c}$ direction of the high temperature NdWO tetragonal variety, or the $\vec{c}$ direction of the high temperature polymorph α-LaWO, orthorhombic.[26] Indeed, the two high temperature varieties (NdWO-tetragonal and LaWO orthorhombic) are strongly related, and only the a parameter differs between them: $a_{LWO\text{-}ortho} \sim 3 \times a_{NdWO\text{-}tetra}$; $b_{LWO\text{-}ortho} \sim b_{NWO\text{-}tetra}$; $c_{LWO\text{-}ortho} \sim c_{NWO\text{-}tetra}$. However, at this step, and considering only the *00l* peaks, it is not possible to discriminate them.

In the case of La_2WO_6,[26] we have already shown that starting from a target containing the low temperature polymorph, PLD technique stabilizes the high temperature polymorph. It is important, in the present unknown case of Nd_2WO_6, to conclude on the true symmetry of the structure and know if the film is either tetragonal or orthorhombic. In addition, if the majority of the diffraction peaks can be attributed to only one **c**-axis growth direction, the two peaks at 2θ = 32.47° and 68.13°, attributed to (5 1 0) and (10 2 0) orientations respectively, indicate that crystallites are also growing in another direction with respect to the plane of the substrate. It is possibly due to the increasing refractory behavior of Nd compared to La, and the fact that the maximum of temperature that our heater can reach is T_{max} = 900°C. To answer this open complex question, we decided to make a complete XRD study.

Considering a_{STO} = 3.905 Å for commercial STO substrates (Crystal GmbH), and $a_{NdWO} = b_{NdWO}$ = 5.426 Å (by referencing to the Yoshimura results on the tetragonal NdWO form), [31] the lattice mismatch between the film and the substrate can been calculated as follows:

$$\delta = \frac{aSTO \times \sqrt{2} - aNdWO}{aSTO \times \sqrt{2}} \times 100 \qquad \text{Equation [1]}$$

The quite low value of the lattice mismatch, δ=1.7%, *i.e.* meaning low tensile strains induced by the substrate in the plane of the film, indicates a possible matching of a_{NdWO} on a (001)-STO allowing an expected good crystalline quality of the thin film growth.

Epitaxy relationship

In order to further investigate the thin film quality, rocking curves on both 001 peak of the STO substrate and 002 peak of the NdWO thin film were recorded (**Figure 2b**). The 0.17° full width at half-maximum (FWHM) value measured for NdWO, with respect to the 0.07° one obtained for the substrate, indicates a relatively good crystalline quality with a weak disorientation of the coherent domains observed along the ***c***-axis thin film growth direction.

To get better insight in the characterization of the microstructural properties of our NdWO thin films, φ scan of the 101 and 011 reflections in the tetragonal hypothesis (in green on the **Figure 3**) indexed as 301 and 011 with orthorhombic hypothesis (in black on the **Figure 3**), have been recorded. Those specific reflections were chosen because of their relatively high intensities and their position quite isolated from substrate's ones. Whatever the symmetry, these planes diffract at $2\Theta_{Bragg}$ = 19.19° and the χ angle between (001) and (301)/(011) is 59.25° (calculated from Carine software [40]). As expected for an epitaxial growth, four peaks are observed on these scans, with a 90° angular-gap between two consecutive ones, in agreement with simulation made by Stereopole software in the case of tetragonal or orthorhombic symmetry. [41]

Unfortunately, at this step, it is still not sure if the NdWO thin film crystallizes either in the tetragonal cell or in the 3×a superstructure orthorhombic. In order to verify this point, a RSM was recorded on the area of the assumed 521 reflection, peak that exists only if the cell is orthorhombic (it would lead to a non-integer 2.5 2 1 peak in the tetragonal hypothesis). Since, we observed some non-negligible intensity in this area, it proves that the NdWO thin film is orthorhombic (**Figure 4a)**.

In a second time, we located the exact positions (after optimization of the φ and χ angles) of the 301 ($2\theta = 19.22°$) and 011 ($2\theta = 19.20°$) reflections in order to extract the *a* and *b* cell parameters of the film. The *c*-lattice parameter value was indeed previously calculated from the 2θ-ω diffractogram given in **Figure 2a**, *i.e.* $c = 8.68$ Å. The *a* and *b* film parameters were deduced from the 2θ values, leading to 16.34(5) Å and 5.46(5) Å respectively. By comparison with the ones of α-LaWO ($a = 16.56(1)$ Å, $b = 5.72(1)$ Å; $c = 8.87(1)$ Å), an 8% decrease of the cell volume is observed. This is in accordance with the evolution observed for the cell volume of the Ln_2WO_6 series with the rare earth radii.

Finally, to investigate the "clamping" state of α-NdWO thin film on the substrate, a last RSM was recorded around the [001]* node of the STO, close to the [002]* node of the film: a perfect vertical alignment between the thin film and the substrate is observed (**Figure 4b**). It means that the film is perfectly clamped on the substrate, in other words that substrate imposes its in-plane parameters to the in-plane ones of the film.

Epitaxial relationships were deduced from examination of the pole-figure measurements on the 315 film 2θ position, position that allowed to observe on the same figure both 315 peaks from the film and 112 reflection from the substrate. The comparison between the observed and calculated density of poles, using the Stereopole software, [41] shows that NdWO thin film adopts the following epitaxial relationships: $[100]_{NdWO} \parallel [110]_{STO}$, $[010]_{NdWO} \parallel [1\bar{1}0]_{STO}$ and $[001]_{NdWO} \parallel [001]_{STO}$ (**Figure SI1)** *i.e.* the same 3-D heteroepitaxy as α-LWO.

Concerning the (510)-orientation of crystallites with respect to the plane of the substrate, the lattice mismatch was also calculated using the following formula with $c_{NdWO} = 8.695$ Å:

$$\delta' = \frac{aSTO \times \sqrt{5} - cNdWO}{aSTO \times \sqrt{5}} \times 100 \qquad \text{Equation [2]}$$

As a result, the value of the lattice mismatch is very low, δ' = 0.4% meaning $[001]_{NdWO} \parallel [210]_{STO}$. However, no clear relationship in the perpendicular direction in the plane of the substrate is evidenced between $[5\bar{1}0]_{NdWO}$ and $[1\bar{2}0]_{STO}$. This could explain the (00l)-preferential growth of the film when optimized deposition conditions are performed as reported for LWO films. [26] As previously reported, we believe that the temperature of deposition, too low with our deposition system, is the cause of the coexistence of these two orientations. Nevertheless, as observed on **Figure 5**, the rocking curve measured on the 510 peak is on the same order of value as the one measured on the 003 peak meaning a similar crystallization of these (510)-oriented crystallites compared to the (00l)-oriented ones.

Figure 6a presents a TEM image of the thin film cross-section, while inset picture is a high-resolution image of the lattice at the interface, confirming that the film is epitaxially grown. **Figure 6b** shows Fourier transforms calculated in the three regions indicated by squares. The region number 1 corresponds to the STO substrate. The regions number 2 and 3, in the film, correspond to domains with two different orientations. As already pointed out on the 2θ-ω XRD scan (**Figure 3a**), beside *00l* peaks, 510 and 10 2 0 peaks are observed, allowing easy identification of the spots in the vertical direction. Thus, regions number 2 and 3 correspond to a (510) and a (001) orientation, respectively. **Figure 6c** presents a color-coded map showing the distribution of the two types of domains in the layer, identifiable by triangular or trapezoidal shape on the image for the (510)-oriented domains. It appears that these (510)-domains (red color) are randomly distributed in the (001)-oriented matrix (green color), except at the interface with the substrate, where the (510) orientation is preferred.

In order to obtain more information about the residual strain distribution, lattice deformation maps were calculated from the image in **Figure 6a** using geometrical phase analysis. [36] **Figure 6d-f** show maps of the horizontal deformation (E_{xx}), vertical deformation (E_{yy}) and shear deformation ($E_{xy}+E_{yx}$), where the deformation is defined with respect to the substrate lattice. **Figure 6g** shows profiles extracted from the maps along the vertical dashed arrows. The horizontal deformation E_{xx} shows no strong variation at the bottom interface and at the domain walls.

It confirms that the lattice of the layer is epitaxially aligned onto the substrate one and that domain walls are also coherent. On the other hand, the E_{xx} profile in **Figure 6g** shows that deformation becomes slightly negative away from the interface (in average -2% between 50 and 150 nm). It indicates that mismatch strain between NdWO and STO (estimated to δ=1.7%, see equation 1) is gradually relaxed along the growth direction. The vertical deformation map E_{yy} measures the (004) and (510) interplanar distances of the NdWO film with respect to the (002) interplanar distance of the STO substrate. Based on the lattice parameters of the film found using XRD (a = 16.34Å, b = 5.46 Å, c = 8.68 Å) and the lattice parameter of STO (a = 3.905 Å), the corresponding deformations can be calculated theoretically as follows $E_{NdWO(004)} = (d_{NdWO(004)}-d_{STO(002)})/d_{STO(002)}$ = 11% for the (001)-oriented domains and $E_{NdWO(510)} = (d_{NdWO(510)}-d_{STO(002)})/d_{STO(002)}$ = 43% for the (510)-oriented domains. The deformations measured experimentally are 39%±2% and 13%±2% in the (510) and (001) domains respectively, which is in quite good agreement with the theoretical values. The shear deformation map $E_{xy}+E_{yx}$ is uniform and close to zero over the whole image. This is another indication that lattices of both layer and substrate are well aligned.

On the other hand, during the cooling process of the thin film synthesis, some thermal mismatches could overcome due to differences between the substrate and film thermal expansion coefficients (TEC). As evocated, this NdWO polymorph has never been stabilized, consequently no α-NdWO TEC is known. As demonstrated by the present structural thin film characterization, α-NdWO and α-LWO are isostructural. Previously α-LWO bulk TEC has been determined to be around 9.8×10^{-6} Å.°C^{-1}, [25] and by extrapolation, it is reasonable to consider an α-NdWO TEC in the same order than the α-LWO one. As reminder the STO TEC is around 9.4×10^{-6} Å.°C^{-1} which is near to the film one leading to a parallel thermal dilatation between the thin film and the substrate limiting the texturation (see **Figure SI1**) and the cracks of the thin film.

As a partial conclusion of this detailed structural and microstructural study, we showed that, by leveraging the PLD method, it is possible to stabilize a new Nd_2WO_6 polymorph, isostructural to α-La_2WO_6, which we will hereafter name α-Nd_2WO_6.

Nanoscale piezo-/ferroelectric properties

AFM surface morphology of the synthesized film is presented on **Figure 7a**. The 8×8 μm^2 area shows distinct grains and grains boundaries. The grains present irregular shapes with lateral sizes between 100 and 900 nm and a root mean square roughness about 3.6 nm. Nanoscale piezo-/ferroelectric properties have been investigated using PFM tool. Both phase and amplitude loops, recorded in remnant mode for minimizing the electrostatic contribution, are depicted in the inset of the **Figure 7a**. Clear hysteresis with two opposite ferroelectric states are observed from the phase signal with almost 180° phase difference, while typical butterfly-shape is recorded for amplitude response, suggesting local ferroelectricity under the probing tip. However, in the last years, much attention was paid to curious PFM responses recorded on oxide films, *i.e.* classical PFM loops obtained on non-ferroelectric material, which can be attributed to several phenomena such as Joule heating, electrostriction, chemical dipole, charge injection, field effect, Vegard strain, deposition, subsurface damaging, surface damaging or vacancy ordering. [42, 43, 44, 45, 46, 47, 48, 49, 50] Thus, considering the complex nature of the physicochemical phenomena that can exist in such oxide thin films exposed to high electric fields and to accurately verify the ferroelectric-like behavior measured, further PFM analyses were conducted to really confirm that the present response is indeed due to ferroelectricity and not an artifact. More precisely, two strategies currently proposed in the literature were adopted: they consist of probing the bias- and time-dependent hysteresis measurements, as reported by Strelcov *et al.* and Chen *et al.*, respectively. [51],[52] In this way, PFM voltage spectroscopy experiments under different AC driving were firstly carried out. **Figure 7d** displays the evolution of the phase signal by increasing the driving voltage. As observed, the piezoloops are insensitive to the V_{AC} probing voltage as long as the magnitude is lower than the coercive voltage (~5 V), while we note both a narrowing of the hysteresis for applied V_{AC} higher than the coercive voltage and the collapse of the loops. This is due to the flipping of the polarization during the experiments which disturbs the PFM signal at such high driving voltages, which agrees with a ferroelectric switching phenomenon, as already shown. [42, 51] A time-dependent hysteresis study was also undertaken and the results are depicted on the **Figure 7e**. No dependence of the amplitude PFM signal with respect to the cycling period is observed, consistent with a ferroelectric polarization switching process. This behavior enables to exclude an ionic movement under the probing tip which could occur for longer periods, and thus focus on the dynamics of intrinsic polarization as main factor for the amplitude signals recorded, as previously published. [52, 53] These bias- and time-dependent hysteresis measurements represent an essential step to ascribe the hysteresis loops measured by spectroscopic PFM to a pure ferroelectric polarization.

From spectroscopic PFM measurements, the surface deformation amplitude was plotted as a function of various driving AC voltages in order to further confirm the electromechanical nature of the detected signal. As seen on the **Figure 7f**, a linearity is obtained until about 2 V then a saturation is observed, attesting of the piezo-activity of the layer. In the PFM mode, the local deformation amplitude A measured by the probing tip is proportional to the amplitude of the AC voltage V_{AC}, the quality factor Q and the effective piezoelectric coefficient d_{33}^{eff}, *i.e.* $A = d_{33} \times V_{AC} \times Q$. For contact resonance, the amplitude signal is enhanced and Q is usually ranging from 30 to 100,[54] but for such inorganic NdWO compound the loss is considered as rather low which leads to a high value for Q, typically of about 70–100. Considering the slope of the positive linear part of the plot in **Figure 7f** is 185 pm/V (the linearly fitted line leads to $y = 185x$ with $r^2 = 0.9762$), we can estimate the effective piezoelectric coefficient between 1.9 and 2.6 pm/V. Note that it is only an estimation and that it is important to consider that the amplitude response is strongly dependent of the measurement location over the free surface of the film. Besides, the clamping of the film on the substrate can lead to an underestimation of the determined value. In addition, it is also well-known that the electric field beneath the AFM probing tip is inhomogeneous in such PFM experiments, leading to quantitative measurements of signal particularly difficult. [55] However, the essential point to keep in mind is that even if it is not possible to give an accurate value for the local d_{33}^{eff}, the estimated value we measured for deformations (1.9-2.6 pm/V) are promising in view of the development of future lead-free piezoelectric systems based on Ln_2WO_6 family.

Switching behavior was then studied by means of poling experiments using PFM lithography. Artificial domains were locally induced by applying a DC voltage of +10 and –10 V to the AFM tip over rectangular area at the free surface of the film, then out-of-plane PFM signals were measured. As seen on **Figure 7b**, strong bright and dark contrasts are obtained for the phase PFM image corresponding to domains with ‘upward’ (away from the substrate) and ‘downward’ (toward the substrate) polarization, respectively. Amplitude vibration is revealed by the high contrasts seen on the **Figure 7c**, while domain boundaries are highlighted by the absence of amplitude signal due to the switch of polarization. The AFM morphology (**Figure 7a**) simultaneously recorded with PFM images does not reveal any change on the surface, excluding surface electrochemical processes during writing step. [56]

The retention properties of the locally manipulated ferroelectric domains were then investigated. For that, two ‘artificial’ domains with reverse polarization were first formed by applying ±10 V between the AFM tip and the grounded substrate, as revealed by the contrasted out-of-plane PFM phase signal on the **Figure 8b**. The tip-induced polarizations were then probed during one day after poling and the obtained signals are presented on the **Figures 8b-d** (see **Fig. SI2** for detailed signal evolution). First, no correlation is observed between the surface morphology (**Figure 8a**) and the corresponding PFM images (**Figure 8b**), excluding surface reaction to mainly explain such contrasts, while clear blue and yellow contrasts are observed even after 24h. Also, we can observe some regions with lower contrast from 8h after poling, particularly for positively polarized areas (blue regions), and this contrast decreases with time until 24h, suggesting relaxation phenomena, although contrasted areas remain. The study of the time-dependent back-switched domains was performed in view of determining the characteristic time τ which is a strong indication on the parameter governing the PFM contrasts, *i.e.* either intrinsic polarization or mediated by the field-induced ion migration in the bulk of the film. The **Figure 8e** depicts the fraction percentage of switched domains as a function of time. As already reported, we have fitted the relaxation evolution of manipulated domains by means of the following relation:[57, 53]

$$f(t) = fo + Aexp(-\frac{t}{\tau}) \text{Equation (2)}$$

with f(t) the fraction of reversed domain correlated to time t; f_0 the final percentage of written domains and A the final percentage of back-switched domains. The dashed line in **Figure 8e** represents the fitting curve according to **Equation 2** for values of f_0 and A of 90.2 and 9.8%, respectively. We can extract a value for τ of about 30 min which is in good agreement with values already published for other ‘true’ ferroelectric oxides. [57, 53] Such value for the time required to nucleate a reverse domain demonstrates the nonvolatile nature and represents an another proof for ferroelectricity.

Considering both topographic AFM and phase PFM images, relaxed regions (highlighted by the white dotted circles in **Figure 8a)** correspond to surface heterogeneities and especially to the grain boundaries. However, the back-switching does not occur to the created domain walls, in contrast to previous reported studied on other ferroelectrics thin films,[57, 58] except for a relaxation time of about 24h. As a consequence, the common starting point for manipulated domain relaxation seems to be a surface heterogeneity like grain boundaries which act as nucleation sites. This phenomenon was already observed in $Pb(Zr_{0.2}Ti_{0.8})O_3$ thin films.[59] Moreover, it is well-known the grains boundaries present very high default density, such as oxygen vacancy which particularly exist in transition-metal oxides. Numbers of works demonstrated the ferroelectric domain retention was directly impacted by the oxygen defects into the active layer. [60, 61, 62] Indeed, these vacancies play a major role on the domain wall mobility, this mobility being directly related to the relaxation dynamic. Besides, mainly positively manipulated domains (blue contrasts) show relaxation. This can be explained by the presence of surface heterogeneities mentioned above on these poled regions. However, this behavior is mainly supported by the fact that these domains were just positively polarized, while two consecutively reverse polarizations were applied to the other domains. Indeed, some studies have reported a better retention behavior for poled domains when the polarization was reverse switched. [58, 63, 64] Also, the decrease of contrast can be attributed to the depolarization field or owing the domains switched under the tip which might not extend throughout the whole film thickness. [65]

As a consequence, these poling studies both confirm the room temperature stability of the ferroelectricity and reveal a typical behavior of ferroelectric domains relaxation.

Then, from both the specific relaxation behavior for manipulated domains and the inability to perform classical P-E hysteresis measurements on these thin films (mainly due to high current leakages), we undertook to locally probe eventual leakage currents into the NdWO layer. The nanoscale conductivity was measured by using c-AFM technique. Current maps were recorded by scanning the same region with the grounded tip and by varying the bias voltage between –10 and +10 V to the bottom electrode. Images measured at –7 V, –8 V, –9 V and –10 V are presented on **Figure 9b-e**. Differences in conduction properties are observed, as evidenced by the conducting paths in blue contrast. For relatively high voltages (ranging from +10 down to –7 V), the detected current is insignificant, as revealed on **Figure 9b**. From –8 V, local leakage begins to be detected at several locations, corresponding to 'hot spots' (blue regions in **Figure 9c**). By increasing bias (absolute value), most of the existing conducting regions extend and new conducting paths appear as seen on **Figures 9d** and **8e**, indicating the local conductivity is bias-dependent. Black and white dashed circles on the **Figures 9c** and **8e** highlight areas where current clearly extends or where new conducting channels appear, respectively. In addition, obvious correlation between c-AFM contrasts and grain boundaries seen on the associated topographic image (**Figure 9a**) is revealed. Indeed, most of the conductive areas are located between the grains, as particularly observed on **Figure 9e**, while the grain regions do not exhibit significant leakage. A careful interpretation of such current signal located at grain boundaries must be done since a convolution effect with the tip can occur inducing such contrasted areas. Considering the contrasts take only place from a high negative threshold bias, we can reasonably conclude that potential convolution effect between the probe tip and the topography is not the main factor leading to highly conductive zones. Therefore, the local conduction in our NdWO film is found to be mainly dominated by the grain boundaries. Such phenomenon was already observed in ferroelectric oxide thin film as $Pb(ZrTi)O_3$, La-doped $BiFeO_3$ or $BiFeO_3$. [66, 67, 68] The profile of leakage currents with the corresponding topography signal along the same line (dashed yellow line in **Figures 9a** and **e**) is displayed in **Figure 9f**, where an unambiguous correlation between the local conduction and the grain boundaries is demonstrated. In addition, we notice that current intensity is not directly proportional to the depth of the grain boundaries, which excludes the tip-sample convolution as being responsible of the obtained conductivity map. Strong current leakage in grain boundaries involves higher defect density in these zones, such as positively charged oxygen vacancies. Indeed, grain boundaries can act as reservoirs for the accumulation of oxygen vacancies and, as previously mentioned, such transition-metal oxides commonly present high oxygen vacancy rate. [68, 69] Under external bias voltages, a rearrangement of these vacancies occurs which increases their density in the grain boundaries. Consequently, conducting paths appear at these specific locations. Then, by increasing the bias, the charged oxygen vacancies migrate into the NdWO layer in order to reach a new thermodynamic equilibrium, associated to continuous variation of oxygen vacancy distribution. [70] Since the rate of oxygen vacancy diffusion along the grain boundaries is almost five orders of magnitude superior to one of the inner parts of the grains, [67] the current in the grain boundaries increases more rapidly, leading to the specific local current pattern obtained. These observations are very interesting by considering the retention behavior of the polarization discussed above (see **Fig. 8**). Indeed, in both cases the charged defects located at the grain boundaries, and more precisely the oxygen vacancies, can be responsible for the physical phenomena occurring at the nanoscale. As a remark, the observed conduction at grain boundaries is not uniform, *i.e.* each grain boundary does not reveal conductivity. It can be explained by the different degrees of angle mismatch of each grain boundaries owing the two different crystallographic orientations seen on the XRD pattern, namely (001) and (510) (**Figure 2**). Indeed, in this case the strain and interfacial energies should differ for different grain boundaries inducing higher defect density, highlighted by electrical hot spots. [66, 71]

Besides, since our NdWO film presents local ferroelectric properties, the application of the high external bias voltage during c-AFM analyses modifies the electric polarization and gives rise to the growth of ferroelectric domains beneath the tip through the extension of the existing domain walls. By increasing the electric field, the domain walls extend towards the grains center. Since no significant current is detected into the grains, as shown on **Figure 9e**, no conductivity is observed at the typical location of ferroelectric domain walls at the contrary of works focused on $BiFeO_3$ or $PbZrTiO_3$ thin films for example. [72, 73, 74, 75, 76] This is reinforced by the current map measured after the manipulation of ferroelectric domains (see **Figure 7b**), where no change in the current pattern was obtained. Consequently, the local conduction is further confirmed to be mainly grain boundaries dependent.

CONCLUSION

A new polymorph of α-Nd_2WO_6 has successfully been isolated and fully characterized from a structural and ferroelectric point of view. This compound was stabilized in thin film form by taking advantage of the substrate-induced strain during the PLD growth. A particular attention has been paid on the structural characterization of the film by carrying out various experiments by high-resolution XRD including ω-2θ, rocking curves, φ scan, pole figure and RSMs on well-targeted nodes. By carefully choosing a discriminant reciprocal space node, we demonstrated that this new *α*-Nd_2WO_6 polymorph is orthorhombic, isostructural to the high-temperature of bulk *α*-La_2WO_6.[26] By performing bias- and time-dependent PFM hysteresis experiments, and by achieving poling measurements, the local piezo-/ferroelectricity behavior was carefully demonstrated. The room temperature stability of the ferroelectric polarization was also shown. The nanoscale mapping of the conductivity has revealed to be bias-dependent and dominated by the grain boundaries. Higher default density such as the accumulation of charged oxygen vacancies in combination with their good mobility in the grain boundaries under external electric field mainly explained the specific local conduction, as well as the polarization relaxation phenomena observed.

Our results extracted from PFM imaging and spectroscopic mode evidence robust intrinsic ferroelectricity into the NdWO layer at the nanoscale level. This finding extends the piezo-/ferroelectric behavior to a second compound belonging to the A_2WO_6 family (A = lanthanide), the first one being LaWO.[26, 27]

As a consequence, our findings show the strain-engineering as a useful strategy for inducing novel functionalities within oxide thin films, and they particularly allow for extending the class of lead-free ferroelectric materials.

FIGURES.

Figure 1. Temperature-dependence of Nd_2WO_6 bulk crystal-structures. Structure projection of (a) low temperature monoclinic Nd_2WO_6 with [WO_6] blocs; (b) orthorhombic high temperature Nd_2WO_6 allotropic variety with isolated [WO_6] polyhedral and (c) high temperature tetragonal Nd_2WO_6 form which is isostructural to $Nd_{1.2}Lu_{0.8}WO_6$ from Yoshimura results. [31]

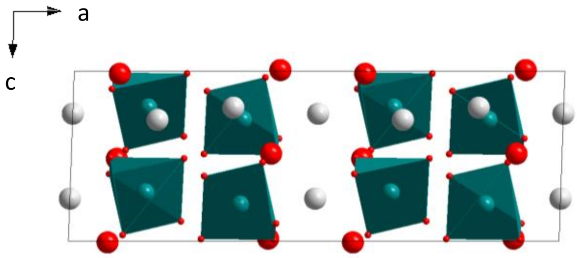

a) **Monoclinic form (T < 1430°C)**
a= 5.55 Å b= 11.38 Å c= 15.86 Å
β= 107.7°

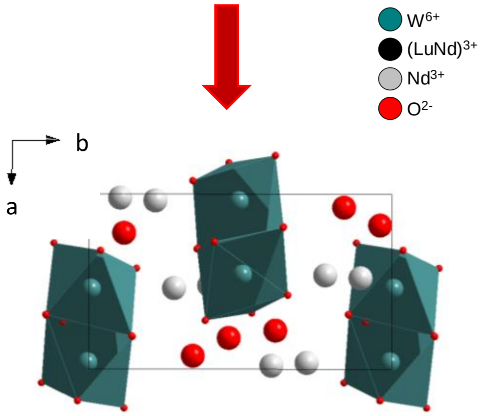

b) **Orthorhombic form (1430°C < T < 1450°C)**
a= 5.536 Å b= 9.231 Å c= 10.170 Å

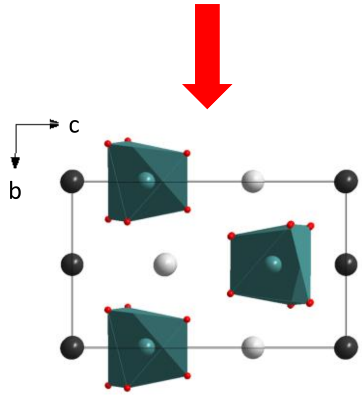

c) **Tetragonal form (T > 1450°C)**
a= 5.426 Å c= 8.695 Å

Figure 2. X-ray diffractograms on Nd_2WO_6 thin films. (a) 2θ-ω X-ray diffractogram of Nd_2WO_6 thin film grown at T= 900°C and $PO_2 = 10^{-1}$ mbar. (b) Normalized rocking curves on 002 NdWO thin film and on 001 STO substrate (FWHM are indicated in inset).

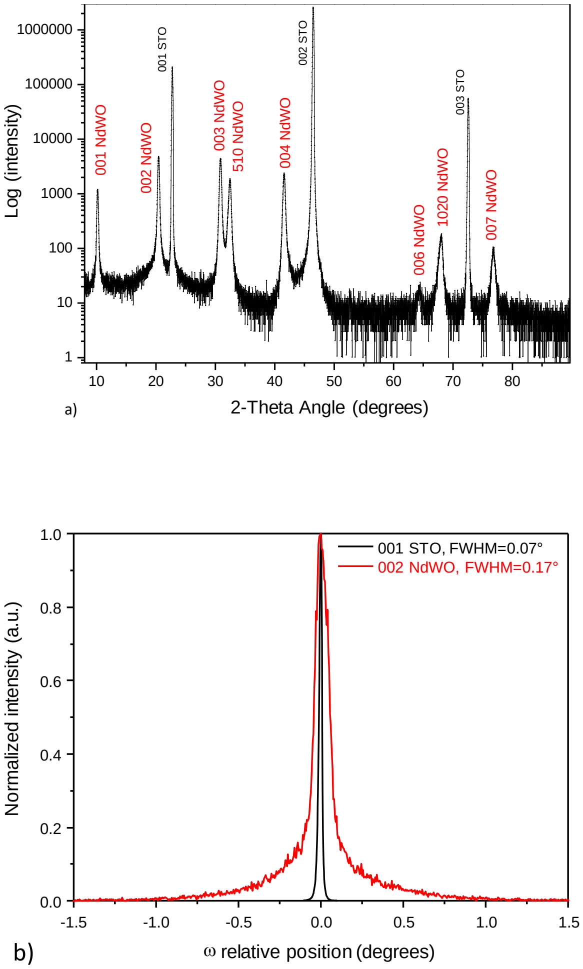

Figure 3. Phi-scan for Nd_2WO_6 on 101/011 peak in case of tetragonal cell (in green) or 301/011 peak on orthorhombic hypothesis (in black). Four peaks are observed; peak repetition rate is 180°.

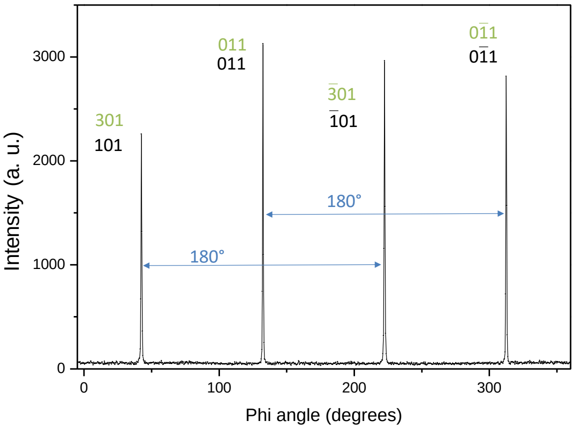

Figure 4. Reciprocal space maps along nodes of NdWO thin film and STO substrate**.** (a) Reciprocal space map along [521]* Nd_2WO_6 highlighting finally the orthorhombic structure of the thin film as α-La_2WO_6. (b) Reciprocal space map, along [001]* STO and [002]* α-NdWO.

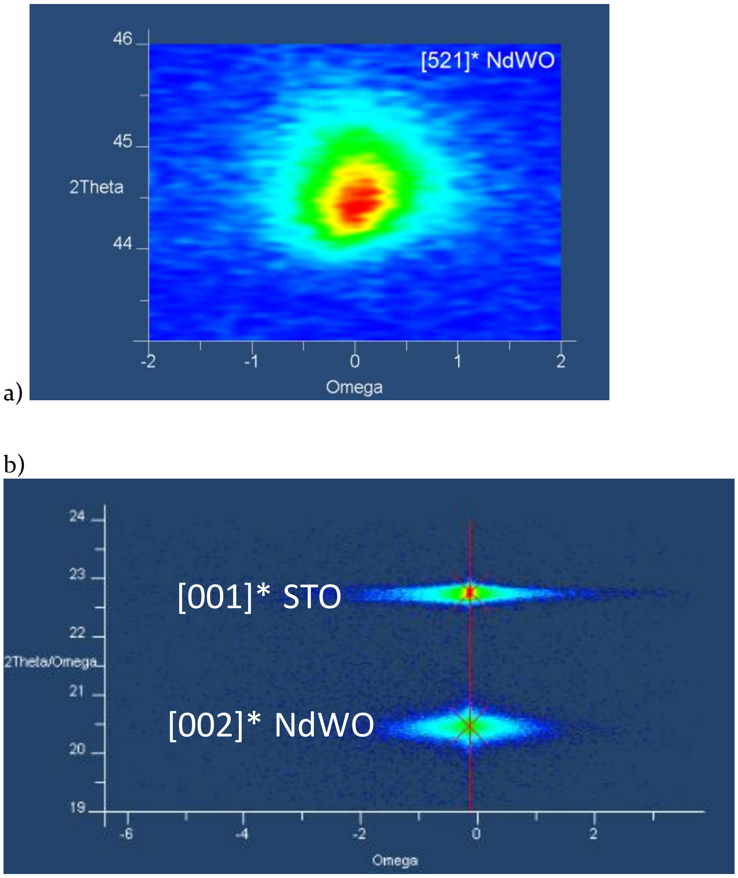

Figure 5. Normalized rocking curves on 003 and 510 NdWO thin film (FWHM are indicated in inset).

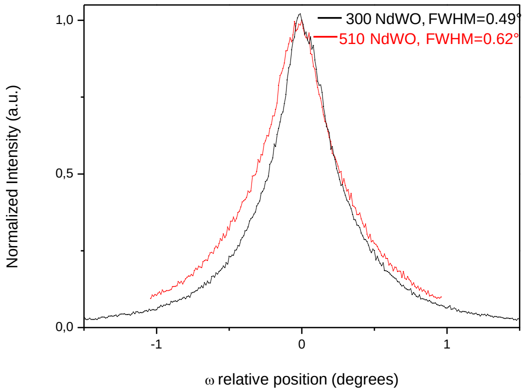

Figure 6. Transmission electron microscopy images of the Nd_2WO_6 film. (a) TEM image of the film cross-section. Inset shows a high resolution image of the epitaxial interface. (b) Fourier transforms obtained in the three regions indicated by squares. (c) Color-coded map that shows the spatial distribution of the two types of domains in the image (a). 510-oriented domains are red and 001-oriented domains are green. The map was created by applying filters to the corresponding spots in Fourier space. (d,e,f) E_{xx} horizontal deformation, E_{yy} vertical deformation and $E_{xy}+E_{yx}$ shear deformation maps obtained using geometrical phase analysis. (g) Deformation profiles extracted from the maps along the dashed arrows.

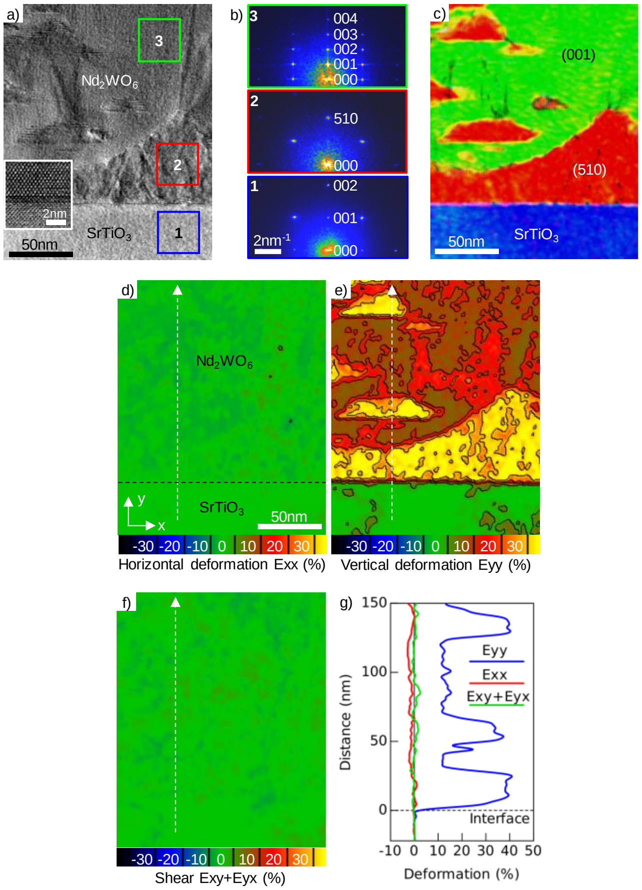

Figure 7. Nanoscale piezo-/ferroelectric behavior and bias- and time-dependent hysteresis measurements properties performed on Nd_2WO_6 thin film. (a) AFM morphology simultaneously measured with out-of-plane (b) phase and (c) amplitude PFM images after poling experiments. The inset of the (a) shows the local remnant phase and amplitude piezoresponse loops recorded on the free surface of the NdWO thin film. (d) Phase PFM loops under different AC driving voltage, (e) and amplitude PFM loops for different period time. (f) AC voltage dependence of the local surface displacement of the NdWO layer. The regression plot between 0 and 2 V corresponding to the linear part (highlighted by the blue rectangular) leads to an effective piezoelectric coefficient between 1.9 and 2.6 pm/V.

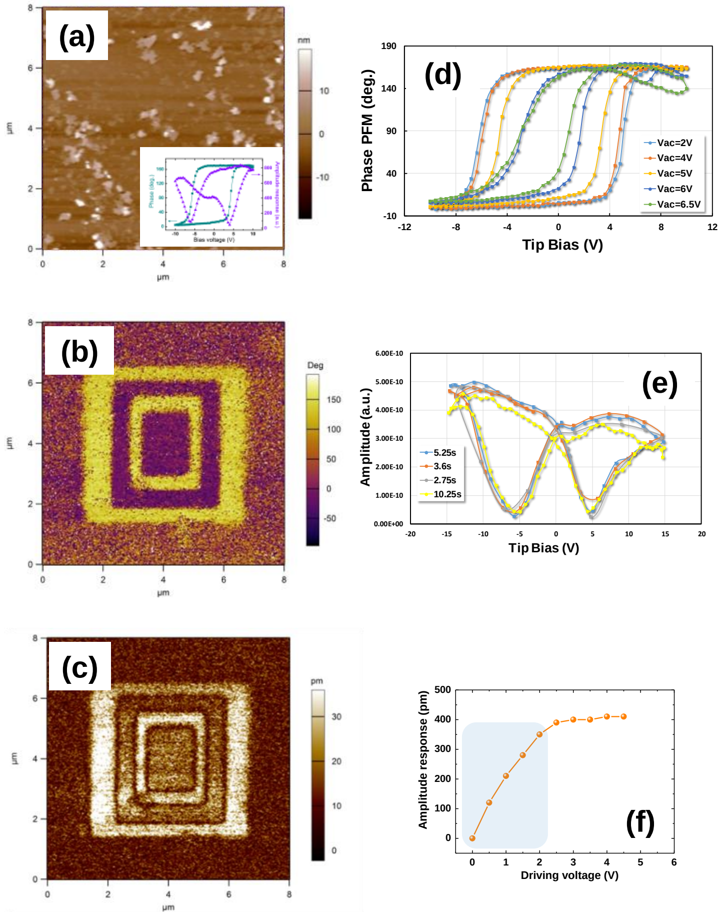

Figure 8. Time-dependence of the locally manipulated domains. (a) AFM morphology and out-of-plane phase PFM signals recorded (b) just after, (c) 8h after, and (d) one day after the poling experiment at ±10 V. Scale bars of phase signal are similar for all of PFM images. White dotted circles on AFM image denote the surface heterogeneities acting as nucleation sites for reverse domains. (e) Percentage of reversed domains as a function of time. Dashed line corresponds to the fitting curve according to **Equation 2**, leading to characteristic time value of about 30 min.

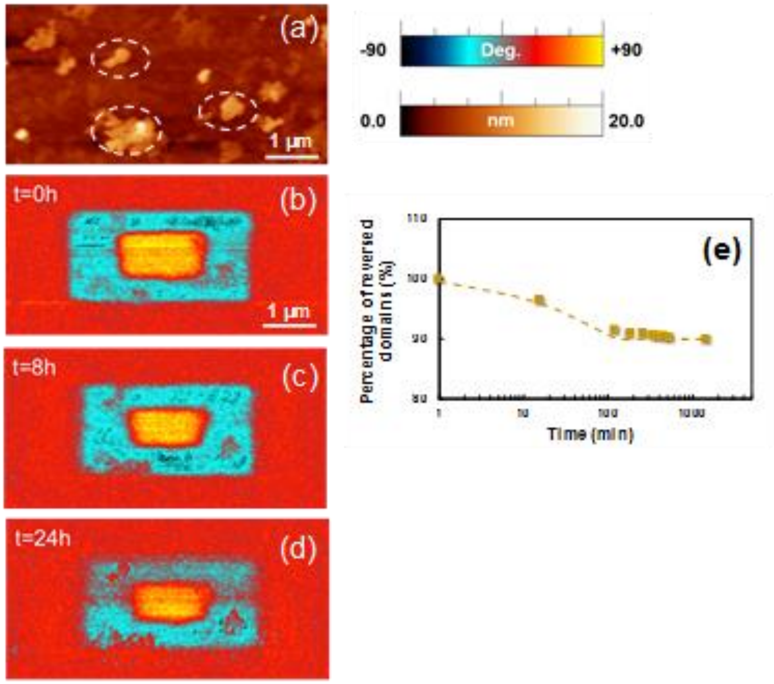

Figure 9. Local conduction in Nd_2WO_6 thin film. (a) AFM topography, and current maps of the corresponding NdWO surface recorded with bias voltages of (b) −7 V, (c) −8 V, (d) −9 V and (e) −10 V. Higher conductivity is detected when larger bias voltage is applied. (f) Current signal and associated topography profile along the yellow dotted lines in (a) and (e), indicating the correlation between the local leakages and the grain boundaries. Scale bars for the current intensity are similar for all c-AFM images.

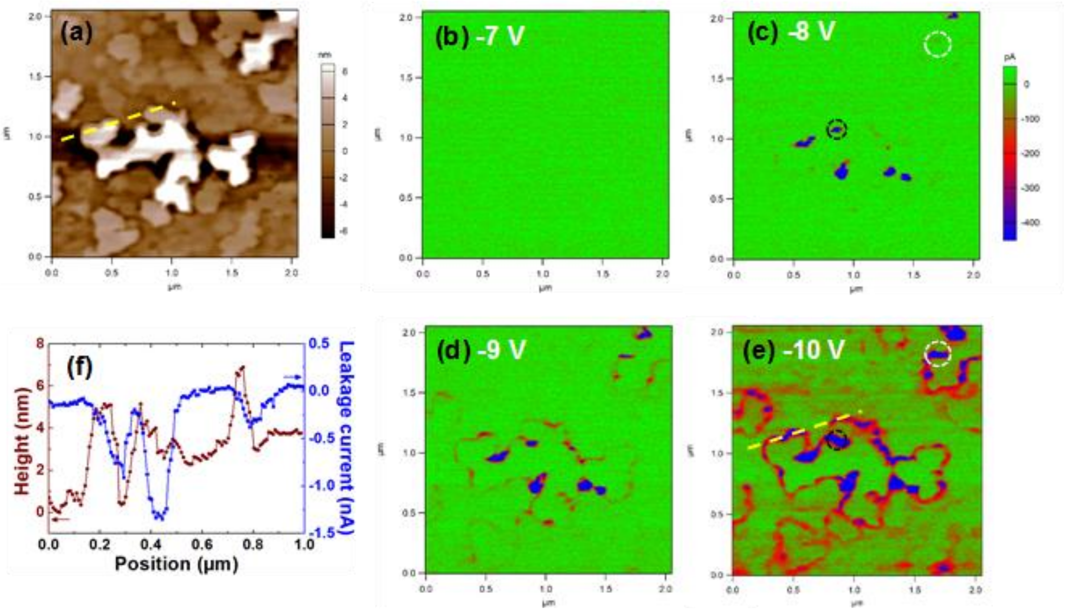

AUTHOR INFORMATION

Corresponding Author

* MH Chambrier : mhelene.chambrier@univ-artois.fr

Author Contributions

The manuscript was written through contributions of all authors. / All authors have given approval to the final version of the manuscript. / ‡These authors contributed equally.

ACKNOWLEDGMENT

The authors would like to acknowledge L. Maës for his technical support and A. Verbeke for her help on powder synthesis.

Chevreul Institute (FR 2638), Ministère de l’Enseignement Supérieur, de la Recherche et de l’Innovation, Hauts-de-France Region, Fonds Européen de Développement Régional (FEDER) and Major Domain of Interest (DIM) "Eco-Energy Efficiency" of Artois University are acknowledged for supporting and funding partially this work. FEDER, CNRS, Hauts-de-France Region and Ministère de l'Education Nationale de l'Enseignement Supérieur, de la Recherche et de l’Innovation are acknowledged for fundings of X-ray diffractometers. Région Hauts-de-France and FEDER are gratefully acknowledged for funding the MFP-3D microscope under Program “Chemistry and Materials for a Sustainable Growth”.

REFERENCES

---

[1] Nagarajan, V.; Roytburg, A.; Stanishevsky, A. ; Prasertchoung, S., Zhao, T.; Chen, L.; Melngailis, J. ; Auciello, O.; Ramesh, R. ,Dynamics of Ferroelastic Domains in Ferroelectric Thin Films. *Nat. Mater.* **2002,** 2, 43-47.

[2] Vrejoiu, I.; Le Rhun, G.; Pintilie, L.; Hesse, D.; Alexe, M.; Gösele, U., Intrinsic Ferroelectric Properties of Strained Tetragonal $PbZr_{0.2}Ti_{0.8}O_3$ Obtained on Layer-by-Layer Grown, Defect-Free Single Crystalline Films. *Adv. Mater.* **2006,** 18, 1657-1661.

[3] Leclerc, G. ; Domengès, B.; Poullain, G.; Bouregba, R., Elaboration of (111)-oriented La-doped PZT Thin Films on Platinized Silicon Substrates. *Appl. Surf. Sci.* **2006**, 253, 1143-1149.

[4] Detalle, M.; Ferri, A.; Da Costa, A.; Desfeux, R.; Soyer, C.; Rémiens, D.,Nanoscale Study by Piezoresponse Force Microscopy of Relaxor $0.7Pb(Mg_{1/3}Nb_{2/3})O_3$-$0.3PbTiO_3$ and $0.9Pb(Mg_{1/3}Nb_{2/3})O_3$-$0.1PbTiO_3$ Thin Films Grown on Platinum and $LaNiO_3$ Electrodes. *Thin Solid Films* 2010, 518, 4670-4674.

[5] Saito, Y.; Takao, H.; Tani, T.; Nonoyama, T.; Takatori, K. ; Homma, T.; Nagaya, T.; Nakamura, M. Lead-free piezoceramics, *Nature* **2004** ,432, 84-87.

[6] Shvartsman, V. V.; Pertsev, N. A ; Herrero, J.M.; Zaldo, C.; Kholkin, A. L. Nonlinear local piezoelectric deformation in ferroelectric thin films studied by scanning force microscopy, *Journal of Applied Physics* **2005**, 97,104105.

[7] Zhang, S.; Xia, R.; Shrout, T. R. Lead-free piezoelectric ceramics vs. PZT? *Journal of Electroceramics* **2007**, 19, 251-257.

[8] Uchino, K. Ferroelectric devices; Taylor and Francis Group, 2010.

[9] EU-Directive 2002/96/EC: Waste Electrical and Electronic Equipment (WEEE); *Off. J. Eur. Union* **2003,** 46, [L37], 24–38.

[10] EU-Directive 2002/95/EC: Restriction of the Use of Certain Hazardous Substances in Electrical and Electronic Equipment (RoHS); *Off. J. Eur. Union* **2003,** 46, [L37], 19–23.

[11] Rödel, J.; Jo, W.; Seifert, K. T. P.; Anton, E.-M.; Granzow, T. Perspective on the development of Lead-Free Piezoceramics. *J. Am. Ceram. Soc.* **2009**, 92 [6], 1153-1177.

[12] Wu, J.; Xiao, D.; Zhu**,** J. Potassium−Sodium Niobate Lead-Free Piezoelectric Materials: Past, Present, and Future of Phase Boundaries. *Chemical Review* **2015,** 115, 2559-2595.

[13] Borchardt, H.J.; Bierstedt, P. E. Ferroelectric Rare Earth Molybdates. *J. Chem. Phys.* **1967**, *38*, 2057-2060.

[14] Flippen, R. B.; Hogan, E. M. Mechanical transducers using coupled ferroelectric-ferroelastic crystals, *US Patent* Appl N°428,717, **1973**.

[15] Lu, H.; Lee, D.; Klyukin, K.; Tao, L.; Wang, B.; Lee, H.; Lee, J.; Paudel, T. R.; Chen, L.-Q.; Tsymbal, E. Y.; Alexandrov, V.; Eom, C.-B.; Gruverman; A. Tunneluing Hot Spots in Ferroelectrics SrTiO3,. *Nano Lett.* **2018,** 18, 491-497.

[16] Brixner, L. H.; Sleight, A. W.; Foris, C. M. Refined Cell parameters of the Ln_2WO_6-Type Rare Earth Tunsgates. *J.of solid States Chem.* **1973**, 7, 418

[17] Efremov, V. A.; Tyulin, A. V. Polymorphism of Oxytungstates Tr_2WO_6. Mechanism of Structural Changes of Er_2WO_6. *Kristallografiya* **1987**, *32*, 363-370.

[18] Efremov, V. A.; Tyulin, A. V. Polymorphism of Oxytungstates Tr_2WO_6. Analysis of Structural Type II (Gd_2WO_6 and Gd_2MoO_6). Mechanism of Structural Change in Gd_2WO_6 in the Phase Transition II <-> V. *Kristallografiya* **1987**, *32*, 371-377.

[19] Polyanskaya, T. M.; Borisov, S. V.; Belov, N. V. A New Form of the Scheelite Structural Type: Crystal Structure of Nd_2WO_6. *Dokl. Akad. Nauk SSSR* **1970**, *193*, 83-86

[20] Tyulin, A. V.; Efremov, V. A.; Trunov, V. K. Polymorphism of Oxytungstates Tr_2WO_6. Mechanisms of Structural Changes in Y_2WO_6. *Crystallogr. Rep.* **1989**, *34*, 531-536.

[21] Borchardt, H. J. Rare-Earth Tungstates and 1:1 Oxytungstates. *Journal of Chemical Physics* **1963**, 39, 3, 504.

[22] Efremov, V. A.; Tyulin, A. V.; Trunov, V. K.; Kudin, O. V.; Yanovskii, V. K.; Voronkova, V. I. The Crystal Structure of Monoclinic Y_2WO_6 and Yb_2WO_6. *Kristallografiya* **1984**, *29*, 904-909.

[23] Efremov, V. A. Characteristic features of the crystal chemistry of lanthanide molybdates and tungstates. *Russian Chemical Reviews* **1990**, 59 (7), 627-642.

[24] Chambrier, M-H.; Kodjikian, S.; Ibberson, R. M.; Goutenoire, F. Ab-initio Structure Determination of β-La_2WO_6. *J. Solid State Chem.* **2009**, *182*, 209-214.

[25] Allix, M.; Chambrier, M. H.; Veron, E.; Porcher, F.; Suchomel, M.; Goutenoire, F. Synthesis and Structure Determination of the High Temperature Form of La_2WO_6. *Cryst. Growth Des.* **2011**, *11*(6), 2528-2539.

[26] Carlier, T.; Chambrier, M.-H.; Ferri, A.; Estrade, S.; Blach, J.F.; Martin, G. ; Meziane, B.; Peiro, F.; Roussel, P.; Ponchel, F.; Rémiens, D.; Cornet, A.; Desfeux, R. Lead-Free α-La_2WO_6 Ferroelectric Thin Films. *ACS Appl. Mater. Interfaces 2015,* **7**, 24409-24418.

[27] Carlier, T.; Chambrier, M.-H.; Ferri, A.; Bayart, A.; Roussel, P.; Saitzek, S.; Desfeux, R. Microstucture and local electrical investigation of lead-free α-La_2WO_6 ferroelectric thin films by piezoresponse force microscopy. *Thin Solid Films* **2016**, 639, 841-851.

[28] Apostolov, Z. D.; Sarin, P.; Hughes, R. W.; Kriven, W. M. Thermal Expansion of Ln_6WO_{12} and Ln_2WO_6 -An *In Situ* Synchrotron X-ray Diffraction Study. *J. Am. Ceram. Soc.* **2014**, *97*, 2496-2505.

[29] Zhijun, Z.; Hui, Z.; Jun, D. C.; Lin, Y. J.; Xiaojun, W.; Bang, X. D.; Hong, C. H.; Tai, Z. J. Structure refinement Lu_2WO_6 and luminescent properties of Eu^{3+}, Pr^{3+} doped Lu_2WO_6. *J. of Alloys and Compounds* **2008**, *466*, 258-263.

[30] Beaury, O. ; Faucher, M.; Teste de Sagey, G.; Caro, P. Investigation of a new structural type for Y_2WO_6. *Mat. Res. Bull.* **1978**, 13, 953-957.

[31] Yoshimura, M.; Sibieude, F.; Rouanet, A.; Foëx, M. Polymorphism of R_2O_3-WO_3 (R = Rare Earth) compounds at high temperatures. *Rev. int. Htes Temp. et Réfract*. **1975**, 12, 215.

[32] Efremov, V.A.; Tyulin, A. V.; V. K. Trunov. The structure of a new modification of Nd_2SO_6, Kristallografiya **1984**, 29, 673-676.

[33] Meier, S. F.; Schleid, Th. Crystal structure of dineodymium(III) hexaoxotellurate(VI), Nd_2TeO_6. *Z. Kristallogr. NCS* **2004**, 219, 359-360.

[34] Yoshimura, M ; Rouanet, A. ; Sibieude, F. ; Foex, M. Phases de haute température des tungstates de lanthanides du type Ln_2O_3-WO_3 (Ln = La, Ce, Nd, Sm, Dy et Y). *C. R. Acad. Sci. C. Fr.* **1974**, 279, 863-865.

[35] Tyulin, A. V.; Efremov, V. A.; Trubov, V. K. Polymorphism of Ln_2WO_6 oxitungstates. Structure of $Nd_{1.2}Lu_{0.8}WO_6$. *Kristallografia* **1989**, 34, [1], 81-86.

[36] Hÿtch, M.J.; Snoeck, E.; Kilaas, R. Quantitative measurement of displacement and strain fields from HREM micrographs. *Ultramicroscopy* **1998** 74, 131.

[37] Rodriguez, B.J.; Callahan, C.; Kalinin, S. V., Proksch, R. Dual-frequency resonance tracking atomic force microscopy. Nanotechnology **2007**, 18, 1-6.

[38] Qiao, H., Seol, D.; Sun, C.; Kim, Y. Electrostatic contribution to hysteresis loop in piezoresponse force microscopy. *Appl. Phys. Lett.***2019**, 114, 152901.

[39] Desfeux, R. ; Ferri, A. ; Legrand, C. ; Maës, L. ; Da Costa, A. ; Poullain, G. ; Bouregba, R. ; Soyer, C. ; Remiens, D. Nanoscale investigations of switching properties and piezoelectric activity in ferroelectric thin films using piezoresponse force microscopy. *Int. J.Nanotechnol.* **2008**, 5, 827–837.

[40]Boudias, C.; Monceau, D. CaRIne Crystallography. Version 3.1. [Senlis]: Software CaRIne Crystallography, **1989**.

[41] Salzmann, I; Stereopole version 1.2 X-Ray Pole Figure Analysis with IDL : software CaRIne **2004**.

[42] Balke, N; Maksymovych, P.; Jesse, S.; Herklotz, A.; Tselev, A.; Eom, C.-B.; Kravchenko, I. I.; Yu, P.; Kalinin, S. V. Differentiating Ferroelectric and Nonferroelectric Electronmechanical Effects with Scanning Probe Microscopy. *ACS Nano* **2015**, 9, 6484-6492.

[43] Vasudevan, R.K.; Balke, N.; Maksymovych, P.; Jesse, S.; Kalinin, S.V. Ferroelectric or non-Ferroelectric: Why So Many Materials Exhibit "Ferroecltricity" On The Nanoscale. *Appl. Phys. Rev.* **2017**, 4, 021302.

[44] Seol, D.; Kim, B.; Kim, Y. Non-Piezoelectric Effects in Piezoresponse Force Microscopy. *Current Applied Physics **2017**,* 17, 661-674.

[45] Martin, S.; Baboux, N.; Albertini, D.; Gautier, B. Interpretation of Multiscale Characterization Techniques to Assess Ferroelectricity: The Case of $GaFeO_3$. *Ultramicroscopy* **2017**, 172, 47–51.

[46] Bark, C.W.; Sharma, P.; Wang, Y.; Baek, S.H.; Lee, S.; Ryu, S.; Folkman, C.M.; Paudel, T.R.; Kumar, A ; Kalinin, S.V.; Sokolov, A.; Tsymbal, E.Y.; Rzchowski, M.S.; Gruverman, A.; Eom, C.B. Switchable Induced Polarization in $LaAlO_3/SrTiO_3$ Heterostructures. *Nano Lett.* **2012**, 12, 1765-1771.

[47] Borowiak, A. S.; Baboux, N.; Albertini, D.; Vilquin, B.; Saint Girons, G.; Pelloquin, S.; Gautier, B. Electromechamical Response of Amorphous $LaALO_3$ Thin Film probed by Scanning Probe Microscopies. *Applied Physics Letters* **2014**, 105, 012906.

[48] Li, C;. Cao, Y.; Bai, Y.; Li, A.; Zhang;, S.; Wu, D. Electromechanical Response from $LaAlO_3/SrTiO_3$ Heterostructures. *ACS Appl. Mater. Interfaces* **2015**, 7, 10146-10151.

[49] Seol, D.; Park, S.; Varenyk, O. V.; Lee, S.; Lee, H. N.; Morozovska, A. N.; Kim, Y. Determination of Ferroelectric Contributions to Electromechanical Response by Frequency Dependent Piezoresponse Force Microscopy. *Sci. Rep.*, **2016**, 6, 30579.

[50] Carlier, T.; Ferri, A.; Saitzek, S.; Huvé, M.; Bayart, A.; Da Costa, A.; Desfeux, R.; Tebano, A. Microstructure and local electrical behavior in $[(Nd_2Ti_2O_7)_4/(SrTiO_3)n]_{10}$ (n = 4-8) superlattices. *RSC Advances* **2018**, 8, 11262.

[51] Strelcov, E.; Kim, Y.; Yang, J. C.; Chu, Y. H.; Yu, P.; Lu, X.; Jesse, S.; Kalinin, S. V. Role of Measurement Voltage on Hysteresis Loop Shape in Piezoresponse Force Microscopy. *Appl. Phys. Lett.* **2012**, 101, 192902.

[52] Chen, Q. N. ; Ou, Y. ; Ma, F. ; Li, J. Mechanisms of Electromechanical coupling in Strain Based Scanning Probe Microscopy. *Applied Physics Letters* **2014**, 104, 242907.

[53] Guan, Z.; Jiang, Z.-Z; Tian1, B.-B. ; Zhu, Y.-P.; Xiang, P.-H.; Zhong, N. ; Duan, C.-G.; Chu, J.-H. Identifying Intrinsic Ferroelectricity of Thin Film with Piezoresponse Force Microscopy. *AIP Advances* **2017**, 7, 095116.

[54] McLachlan, M.A.; McComb, D.W.; Ryan, M.P.; Morozovska, A.N.; Eliseev, E.A.; Payzant, E.A.; Jesse, S.; Seal, K.; Baddorf, A.P.; Kalinin, S.V. Probing Local and Global Ferroelectric Phase Stability and Polarization Switching in Ordered Macroporous PZT. *Adv. Funct. Mater.* **2011**, 21, 941–947.

[55] Gruverman, A.; Alexe, M.; Meier, D. Piezoresponse force microscopy and nanoferroic phenomena, *Nature Communications* **2019**, 10, 1661.

[56] Ievlev, A.V.; Maksymovych, P.; Trassin, M.; Seidel, J.; Ramesh, R.; Kalinin, S.V.; Ovchinnikova, O.S. Chemical Sate Evolution in Ferroelectric Films During Tip-Induced Polarization and Electroresistive Switching. *ACS Applied Materials & Interfaces* **2016**, 8, 29588–29593.

[57] Ganpule, C.S.; Nagarajan, V.; Ogale, S.B.; Roytburd, A.L.; Williams, E.D.; Ramesh, R.Domain Nucleation and Relaxation Kinetics in Ferroelectric Thin Films. *Applied Physics Letters* **2000**, 77, 3275-3277.

[58] Ganpule, C.S.; Roytburd, A.L.; Nagarajan, V.; Hill, B.K.; Ogale, S.B.; Williams, E.D.; Ramesh, R.; Scott, J.F. Polarization Relaxation Kinetics and 180° domain Wall dynamics in Ferroelectric Thin Films. *Physical review B* **2001**, 65, 014101.

[59] Gruverman, A.; Tokumoto, H.; Prakash, A.S.; Aggarwal, S.; Yang, B.; Wuttig, M.; Ramesh, R.; Auciello, O.; Venkatesan, T. Nanoscale Imaging of Domain Dynamics and Retention in Ferroelectric Thin Film. *Applied Physics Letters* **1997**, 71, 3492.

[60] Kitanaka, Y.; Noguchi, Y.; Miyayama, M. Oxygen-Vacancy-Induced 90°-Domain Clamping in Ferroelectric $Bi_4Ti_3O_{12}$ single crystals. *Physical review B* **2010**, 81, 094114.

[61] Yamamoto, K.; Kitanaka, Y.; Suzuki, M.; Miyayama, M.; Noguchi, Y.; Moriyoshi, C.; Kuroiwa, Y. High-Oxygen-Pressure Crystal Growth of Ferroelectric $Bi_4Ti_3O_{12}$ single crystals. *Applied Physics Letters* **2007**, 91, 162909.

[62] Lee, J.H.;. Shin, R.H; Jo, W. Polarization Switching and Relaxation Dynamics of Bismuth layered Ferroelectric Thin Films: Role of Oxygen Defect sites and Crystallinity. *Physical review B **2011**,* 84, 094112.

[63] Kim, T.Y.; Lee, J.H.; Oh, Y.J.; Choi, M.R.; Jo, W. Charge Retention Behavior of Preferentially Oriented and Textured Bi3.25La$_{0.75}$Ti$_3$O12 Thin Films by Electrostatic Force Microscopy. *Applied Physics Letters* **2007**, 90, 082901.

[64] Lee, J. H.; Choi, M. R.; Oh, Y. J.; Jo, W. Local Retention Behaviors of Epitaxial and Polycrystalline $PbMg_{1/3}Nb_{2/3}O_3$-$PbTiO_3$ Thin Films by Scanning Force. Microscopy. *Applied Physics Letters* **2007**, 91, 072906.

[65] Mazet, L.; Bachelet, R. ; Louahadj, L. ; Albertini, D. ; Gautier, B. ; Cours, R. ; Schamm-Chardon, S. ; Saint-Girons, G. ; Dubourdieu, C. Structural Study and Ferroelectricity of Epitaxial $BaTiO_3$ Films on Silicon Grown by Molecular Beam Epitaxy. *J. Appl. Phys.* **2014**, 116, 214102.

[66] Masuduzzaman, M.; Xie, S.; Chung, J.; Varghese, D.; Rodriguez, J.; Krishnan, S.; Alam, M.A. The Origine of Broad Distribution of Breakdown Times in Polycrystalline Thin Film Dielectrics. *Applied Physic Letters* **2012**, 101, 153511.

[67] Zhou, M.-X.; Chen, B.; Sun, H.-B.; Wan, J.-G.; Li, Z.-W.; Liu, J.-M.; Song, F.-Q.; Wang, G.-H. Local Electrical Conduction in Polycrystalline La-Doped $BiFeO_3$ thin Films. *Nanotechnology* **2013**, 24, 225702.

[68] Shen, X.; Yin, K.; Puzyrev, Y.S.; Liu, Y.; Sun, L.; Li, R.-W.; Pantelides, S.T. 2D Nanovaristors at Grain Boundaries Account for Memristive Switching in Polycrystalline $BiFeO_3$. *Advanced Electronic Materials* **2015**, 1, 1500019.

[69] Yan, X.; Li, Y.; Zhao, J.; Li, Y.; Bai, G.; Zhu, S. Roles of Grain Boundary and Oxygen Vacancies in $Ba_{0.6}Sr_{0.4}TiO_3$ Films for Resistive Switching Device Application. *Applied Physics Letters* **2016**, 108, 033108.

[70] Choi, T.; Horibe, Y.; Yi, H.T.; Choi, Y. J.; Wu, W.; Cheong, S.-W. Insulating Interlocked Ferroelectric and Structural Antiphase Domain Walls in Multiferroic $YMnO_3$. *Nature Materials* **2010**, 9, 253–258.

[71] Read, W.T.; Shockley, W. Dislocation Models of Crystal Grain Boundaries. *Phys. Rev.* **1950**, 78, 275.

[72] Seidel, J.; Martin, L.W.; He1, Q.; Zhan, Q.; Chu, Y.-H.; Rother, A.; Hawkridge, M.E.; Maksymovych, P.; Yu, P.; Gajek, M.; Balke, N.; Kalinin, S.V.; Gemming, S.; Wang, F.; Catalan, G.; Scott, J. F.; Spaldin, N.A.; Orenstein, J.; Ramesh, R. Conduction at Domain Walls in Oxide Multiferroics. *Nature Materials* 2009, 8, 229-234.

[73] Farokhipoor, S.; Noheda, B. Conduction Through 71° Domain Walls in BiFeO3 Thin Films. *Physical Review Letters* **2011**, 107, 127601.

[74] Farokhipoor, S.; Noheda, B. Local Conductivity and The Role of Vacancies Around Twin Walls of (001)-$BiFeO_3$ Thin Films. *Journal of Applied Physics* **2012**, 112, 052003.

[75] Guyonnet, J.; Gaponenko, I.; Gariglio, S.; Paruch, P. Conduction at Domain Walls in Insulating $Pb(Zr_{0.2}Ti_{0.8})O_3$ Thin Films. *Adv. Mater.* **2011**, 23, 5377–5382.

[76] Rojac, T.; Bencan, A.; Drazic, G.; Sakamoto, N.; Ursic, H.; Jancar, B.; Tavcar, G.; Makarovic, M.; Walker, J.; Malic, B.; Damjanovic, D. Domain-Wall Conduction in Ferroelectric $BiFeO_3$ Controlled by Accumulation of Charged Defects. *Nature Materials* **2017**, 16, 322-328.